Hydrogenation of bio-oil derived oxygenates at ambient conditions via a two-step redox cycle

Chongyan Ruan,[1,3] Ryota Akutsu,[1,2,3] Kunran Yang,[1] Noha M. Zayan,[1] Jian Dou,[1] Junchen Liu,[1] Arnab Bose[1], Leo Brody[1], H. Henry Lamb[1] and Fanxing Li[1,4, *]

[1]Department of Chemical and Biomolecular Engineering, North Carolina State University, Raleigh, NC, 27605-7905, USA
[2]Chemistry and Materials Division, Department of Textile Science and Technology, Shinshu University, 3-15-1 Tokida, Ueda-shi, Nagano-ken, Japan, 386-8567
[3]These authors contributed equally
[4]Lead Contact
*Correspondence: fli5@ncsu.edu

SUMMARY

A key challenge in upgrading bio-oils to renewable fuels and chemicals resides in developing effective and versatile hydrogenation systems. Herein, a two-step solar thermochemical hydrogenation process that sources hydrogen directly from water and concentrated solar radiation for furfural upgrading is reported. Superior catalytic performance is achieved at room temperature and atmospheric pressure, with up to two orders of magnitude higher H_2 utilization efficiency compared to state-of-the-art catalytic hydrogenation. A metal or reduced metal oxide provides the active sites for furfural adsorption and H_2O dissociation. The *in situ* generated reactive H atoms hydrogenate furfural and biomass-derived oxygenates, eliminating the barriers for H_2 dissolution and the subsequent dissociation at the catalyst surface. The hydrogenation selectivity can be conveniently mediated by solvents with different polarity and metal/reduced metal oxide catalysts with varying oxophilicity. This work provides an efficient and versatile strategy for bio-oils upgrading and a promising pathway for renewable energy storage.

Bio-oils; furfural; solar thermochemical; H_2O splitting; hydrogenation; renewable energy storage

INTRODUCTION

Developing reliable and carbon-neutral energy processes for sustainable fuels and chemicals production is essential for relinquishing fossil fuel dependency[1-4]. Aside from wind and solar, lignocellulosic biomass (i.e., plant dry matter) constitutes one of the most abundant renewable energy sources[5-10]. However, the highly oxygenated nature of lignocellulosic biomass (30-50% oxygen by weight) leads to a low energy density (<19 MJ/kg)[9,11]. Without upgrading through deep hydrogenation, biofuels derived from lignocellulosic biomass are not suitable as transportation fuels or chemical feedstocks. The conventional catalytic hydrogenation-based biomass-to-fuels processes typically require large quantities of molecular hydrogen (up to 0.12 kg H_2 per kg feedstock such as carbohydrates, vegetable oils, and pyrolysis oils)[12]. Cost-effective and sustainable catalytic processes for efficient biofuel upgrading are therefore urgently needed.

Furfural (C_4H_3OCHO) is an important biomass platform molecule derived from lignocellulosic biomass. With more than 280,000 metric tons produced per annum, it has been identified as one of the top 30 building blocks for sustainable chemical transformation due to its inherent advantages of being renewable and widely available[13-19]. Furfural can be converted via hydrogenation and/or selective deoxygenation into a variety of fuel additives and chemicals including 2-methylfuran (2-MF), furfuryl alcohol (FA), 2-methyltetrahydrofuran (2-MTHF), tetrahydrofurfuryl alcohol (THFA), furan and tetrahydrofuran (THF), and so on. The selective removal of furfural's excess oxygen atom is a key step in the upgrading process. Currently, three approaches are employed: catalytic hydrogenation [9,20], catalytic transfer hydrogenation (CTH)[21,22], and electrochemical hydrogenation (ECH)[23,24]. The conventional catalytic hydrogenation processes ($2C_4H_3OCHO$ (furfural) $+3H_2 = C_4H_3OCH_3$ (2-MF) $+ C_4H_3OCH_2OH$ (FA)) utilize molecular hydrogen as the reducing agent given its wide availability and facile activation on metal catalysts. However, the low solubility of molecular hydrogen in the various reaction media (e.g., 0.00016g/100g H_2O and 0.00069 g/100g benzene at 1 atm, 25°C) necessitates high H_2 pressures (10-20 MPa) well in excess of the stoichiometrically required amount[9]. High reaction temperatures (570-670 K) are also required. Although these conventional catalytic hydrogenation processes are well-established, the large carbon footprints associated with H_2 production and purification as well as the substantial infrastructure costs and safety concerns associated with handling high pressure H_2 have motivated the development of more effective methods for furfural hydrogenation. As an alternative to conventional molecular-hydrogen-based processes, CTH employs liquid organic hydrogen donors such as methanol, ethanol, formic acid, acetic acid, etc., to alleviate the safety concern of handling high-pressure H_2 and to enhance the solubility of the hydrogen donor[22]. Even so, usage of these liquid donors requires substantial modifications of the existing hydrogenation infrastructure, such as the addition of separation and recycle units to extract the unconverted hydrogen donor from the reaction mixture. ECH has recently emerged as another appealing method for hydrogenating furfural through its use of protic electrolytes and electricity to produce reactive hydrogen at low temperatures and pressures[12], thereby removing the need for externally supplied hydrogen. While promising results have been achieved, ECH still faces several critical challenges, such as electrode fouling, polymerization side reactions between the furfural products and the electrolyte, and a low faradaic efficiency resulting from the competing hydrogen evolution reaction[24].

Solar thermochemical water splitting (STWS) constitutes a promising pathway for hydrogen production and efficient storage of intermittent solar energy[25-27]. The reactions can be exemplified as follows:

MO_{ox} + concentrated solar power = $MO_{red} + 1/2O_2(g)$ (1)

$MO_{ox} + H_2O = MO_{red} + H_2(g)$ (2)

where MO_{ox} and MO_{red} denote the oxidized and reduced states of a metal oxide, respectively. While promising results have already been achieved, apart from the generation of hydrogen from water, its potential applications in producing renewable fuels and chemicals remains largely unexplored. Here, a two-step solar thermochemical hydrogenation (STCH) scheme that sources hydrogen directly from water and concentrated solar energy for furfural upgrading was proposed and validated. Figure S1a illustrates a simplified schematic of the two-step STCH process. During the upgrading step, a metal or oxygen deprived metal oxide provides the active sites for furan ring adsorption and acts as a bulk source of reduction potential to dissociate H_2O for *in situ* hydrogen generation. The reactive H atoms are highly effective for upgrading furfural and other biomass-derived oxygenates to hydrogenated fuel products. During the regeneration step, the lattice oxygen is abstracted from the reoxidized metal oxide at elevated temperatures with concentrated solar energy, thus completing the reaction cycle. These reactions can be considered respectively as:

$MO_{red} + H_2O + C_4H_3OCHO$ (furfural) = $MO_{ox} + C_4H_3OCH_2OH$ (FA) (3)

MO_{ox} + concentrated solar power = $MO_{red} + 1/2O_2(g)$ (4)

STCH may provide a sustainable alternative to conventional hydrogenation techniques and offer the following potential advantages. 1. Furfural is commercially produced through acid catalyzed transformation of pentoses in water. Separating of furfural from the dilute aqueous furfural solution (ca. 5 wt%) is energy demanding and capital intensive[13]. The STCH scheme can directly utilize a primary furfural water stream as the feedstock at room temperature, thereby avoiding the use of costly separation units and significantly reducing the overall energy demand for the process. 2. STCH eliminates the requirement of external molecular hydrogen, as well as organic hydrogen donors or protic media, and has the potential to produce fuels and chemicals in a carbon-neutral manner. 3. STCH represents an efficient method of harvesting and storing solar energy via hydrogenation of organic compounds, which can enbable significantly increased fuel yields over standalone biomass-to-fuels pathways. 4. The reaction pathway for STCH is fundamentally different from the conventional furfural hydrogenation process since the reactive atomic hydrogen is generated *in situ* on a metal or oxygen deprived metal oxide surface through H_2O splitting instead of through the dissociation of molecular H_2. Therefore, the barriers for H_2 dissolution in the reaction medium, mass transfer, and the subsequent dissociation at the catalyst surface are avoided. Thus, reactions that typically require high temperatures and pressures in conventional systems can readily occur at mild conditions. 5. Controlling the extent of reduction of the metal oxide during the regeneration step can manipulate its reducing potential for H_2O dissociation and the subsequent hydrogenation, adding an additional degree of freedom in tuning the product distribution. 6. The redox catalyst is renewed upon each regeneration half cycle, avoiding potential long-term carbon deposition, which is generally encountered in conventional catalytic hydrogenation processes. It is noted that, in addition to STCH, other sustainable paths for regeneration can also be readily applied in the proposed approach. Examples include electrochemical reduction of the metal oxide or reduction facilitated by another carbonaceous feedstock. This highlights the flexibility of the proposed approach. The current work focuses on the unique hydrogenation step since the reduction half cycle of various redox active oxides have been extensively investigated in the context of metal production[28,29], chemical looping[30-32], and solar thermochemical water or CO_2-splitting[25,26,33,34].

The attractiveness of the STCH technology depends largely upon the thermodynamic and kinetic properties of the redox catalyst, which functions as the redox intermediate for oxygen ion delivery between the two redox half cycles. Recent studies have demonstrated solar thermal or solar electrothermal reduction of Al_2O_3, MgO, ZnO and SnO_2[28,35-39]. For instance, a 100 kWth scale pilot plant for thermal reduction of ZnO has been accomplished with a Zn molar content of as high as 44%[29]. Meanwhile, thermochemical cycles utilizing ceria-based redox materials have exhibited great promise for both H_2O and CO_2 splitting given their relatively low reduction temperature, superior oxygen ion conductivity, and robust structural and crystallographic stability[25,40-44].

Herein, the first demonstration of furfural upgrading via a two-step STCH approach was reported. Oxophilic, zero-valent metals including Zn, Sn, Fe, Al, Mg and Mn, as well as a non-stoichiometric $CeO_{2-\delta}$ redox catalysts, were screened to investigate the feasibility of the proposed process. Notably, efficient upgrading of furfural was achieved at room temperature and atmospheric pressure, with hydrogen utilization efficiency 1-2 orders of magnitude higher than molecular-hydrogen-based hydrogenation processes. By using suitable metal/reduced metal oxide with different oxophilicities, the hydrogenation reaction can be driven exclusively to FA and 2-MF. Mechanistic investigations indicate that zero-valent metals or surface oxygen vacancies are active redox centers for *in situ* generation of reactive hydrogen species from H_2O. Effects of solvent for furfural hydrogenation were investigated using a combined experimental and theoretical approaches. The STCH approach was further extended to the conversion of other biomass derivatives with similar functional groups, exhibiting superior catalytic performance. As such, the proposed approach has the potential to open up new opportunities for sustainable production of fuels and chemicals.

Results and Discussion

Redox Performance

To demonstrate the feasibility of this concept, the redox energetics of metal/metal oxide reaction pairs across the periodic table using the HSC thermochemical database were screened. Figure S2 plots the thermodynamic potentials for water splitting and metal oxide thermal regeneration for 19 metal/metal oxide and 1 reduced metal oxide/metal oxide redox pairs versus temperature. Based on thermodynamic and practical constraints, 7 redox candidates—Zn/ZnO, Sn/SnO, Fe/FeO (FeO/Fe_3O_4), Mn/MnO, $CeO_{1.83}/CeO_2$, Mg/MgO and Al/Al_2O_3 were highlighted, which are suitable for solar thermochemical H_2O splitting or solar electrothermal reduction and investigated their performance for STCH of furfural. As shown in Figure 1a, H_2O splitting is thermodynamic favourable ($\Delta G_{rxn} < 0$) with Zn, Sn, Fe, Mn, $CeO_{1.83}$, Mg and Al in the temperature range of 0-300°C. Sn/SnO exhibits similar redox potentials for H_2O splitting as Fe/FeO (FeO/Fe_3O_4). Mg/MgO and Al/Al_2O_3 show higher oxophilicities and thermodynamic driving forces for H_2O splitting (Figure 1a), but at the expense of a more difficult regeneration, e.g., requiring high temperatures (Figure S2d). $CeO_{1.83}/CeO_2$, Zn/ZnO and Mn/MnO redox pairs intermediate between. The catalytic performance over different catalysts for the two-step STCH of furfural using H_2O as the hydrogen source is summarized in Table S1. At 150°C, furfural was converted exclusively to FA (>99% selectivity) over Al, AlCu alloy (8% Cu), Mn, Fe and Mg. The conversions ranged between 14.2-28.0% (Table S1, entries 2-6). While for Zn and Sn, 2-MF, FA and THF were the primary products at 150°C, with enhanced furfural conversions for Zn (Table S1, entry 1) despite a lower oxophilicity compared to Al and Mg. Interestingly, the product selectivity shifted to 2-MF (>99%) when employing reduced CeO_2 or 1%Ru/CeO_2 redox catalyst (Table S1, entry 8 and 9). These findings indicate that the nature of the metal/reduced metal oxide is crucial in regulating the product selectivity. It is noted that Zn showed >50% furfural conversion even at room temperature and atmospheric pressure (Table S1, entry 10), while no activity was observed for Al, Mn, Fe, Sn and Mg under identical conditions (Table S1, entries 11-16).

The effects of different solvents on furfural conversion and product distribution for Zn at room temperature were also investigated. As illustrated in Figure 1b, Zn exhibited promising furfural hydrogenation performance in neat H_2O or in different organic solvents using H_2O as the hydrogen source, among which dichloromethane resulted in the highest furfural conversion. Notably, the solvent has a marked effect on product selectivity. In high polarity solvents such as H_2O and a 1,4-Dioxane/H_2O mixture, FA is the primary product. While in lower polarity solvents such as dichloromethane, cyclohexane and dodecane, 2-MF dominates. Similar observations were also reported by Obaid et al.[45] and Sarwat et al.[46] in conventional catalytic hydrogenation, who demonstrated that dichloromethane gave the best catalytic performance for furfural and FA hydrogenation over Pt/TiO_2 catalyst among different solvents, with a high selectivity to 2-MF. A comparison of furfural conversion and product distribution in H_2O, 1,4-Dioxane/H_2O and dichloromethane/H_2O mixture as a function of temperature is summarized in Figure S3. It is interesting to note that the furfural conversions peak at 25 and 50°C. Further increase in reaction temperatures to 100 and 150°C led to a drop in furfural conversion. We attribute it to the competition from the hydrogen evolution reaction (the combination of atomic H to produce molecular H_2 rather than hydrogenation of furfural), which is more favourable at high reaction temperatures. This is supported by the fact that the hydrogen utilization efficiency decreases (defined as the molar ratio of hydrogenation products to the total amount of Zn consumed during the reaction) with increasing temperature (Figure S4). Meanwhile, a significant difference was observed in furanic product selectivity (Figure S3). The hydrogenation of furfural gives predominantly FA in H_2O and 1,4-Dioxane/H_2O mixture, while 2-MF dominates in dichloromethane/H_2O mixture over 25-150°C. These results indicate that the hydrogenation selectivity can also be effectively mediated with different solvents, adding an extra dimension in manipulating the product distribution. Additionally, the effect of reaction time on activity and product distribution over Zn in dichloromethane/H_2O mixture was investigated at 150°C (Figure S5). Furfural conversion and 2-MF selectivity peaked at 4h, reaching 47.6% and 89.3%, respectively. When further increasing the reaction time to 6 and 8h, furfural conversion decreased slightly, which could be attributed to the polymerization of furfural and its adsorption on the catalyst surface as indicated by the decreased carbon balance. Note that the carbonaceous deposits can be removed during the high temperature regeneration half cycle. In conventional catalytic hydrogenation, Chinh et al. demonstrated a complete furfural conversion with a MF selectivity of 50% after 7 h over a Co_3O_4 catalyst (180°C, 20 bar of H_2)[47]. Mohammed et al. showed that the FA selectivity plateaued at 90-100% after 7 h with furfural conversion ranged between 25-60% over Cu-based catalysts (50°C, 20 bar of H_2)[48]. Feiying et al. showed that a close to complete furfural conversion can be achieved with a MF selectivity of 90% after 12h over $NiCu_{0.33}/C$ catalyst (120°C, 15 bar of H_2)[49].

The furanic product yield and H_2 utilization efficiency of Zn in the STCH process was further compared with the conventional molecular-hydrogen-based hydrogenation process over ZnO in H_2O, 1,4-Dioxane/H_2O, and dichloromethane/H_2O mixture at 150°C. As shown in Figure 1c, a two to seven-fold increase in furanic product yield was observed for STCH of furfural over Zn using H_2O as the hydrogen source. These correspond to an eight to eighty-fold increase in hydrogen utilization efficiency compared to the conventional process over ZnO in the presence of high pressure H_2 (~2 MPa). The exceptional hydrogen utilization efficiency indicates that the *in situ* generated atomic H species are significantly more effective for furfural hydrogenation than molecular H_2. No hydrogenation proceeded when using ZnO in the absence of external H_2, suggesting that water dissociation by Zn was a key step for furfural hydrogenation. The hydrogen utilization efficiency was further compared to state-of-the-art catalysts in either liquid or gas phases with molecular hydrogen (Figure 1d, see Table S2 for more details). One to two orders of magnitude higher efficiency were achieved, demonstrating the greater efficacy of the STCH process. The unconverted hydrogen cogenerated for STCH of furfural can be stored, used as a fuel, or a chemical reactant (e.g., to facilitate the reduction of the metal oxide in this process), or recycled to a second catalytic bed to further hydrogenate the remaining furfural (Figure S1b). Note that the current study focuses on the Zn oxidation step to demonstrate its unique effectiveness for hydrogenation reactions. The oxidized ZnO can be converted back to Zn using either the commercial electrolysis approach with renewable electricity or the emerging solar thermochemical decomposition technology[28,29,35,50]. In particular, Steinfeld et al[51] estimated a solar to hydrogen efficiency of 29% through solar thermochemical ZnO reduction. Considering that the current approach demonstrated 1 - 2 orders of magnitude higher H_2 utilization efficiency (compared to state-of-the-art catalytic hydrogenation) and it can be operated at near ambient temperature and pressure, it's anticipated that the overall process efficiency to be notably higher than traditional catalytic hydrogenation irrespective of the source of hydrogen utilized. To establish the generality of this approach, the STCH of various carbonyl containing biofuel surrogates besides furfural (Table 1) were probed. Complete conversions of benzaldehyde and cyclohexanecarboxaldehyde were achieved with exclusive selectivity to their corresponding unsaturated alcohols (Table 1, entries 1 and 3) at 25°C, without hydrogenation of the aromatic rings. For benzaldehyde and cyclohexanecarboxaldehyde, whose structures are similar to furfural, the conversions decreased slightly to 96% and 73%, respectively, when further increasing the temperature to 150°C (Table 1, entries 4 and 6), following similar trends to that of furfural. These results further support the hypothesis that the combination of *in-situ* generated atomic H to produce molecular H_2 competes with hydrogenation at higher temperatures.

Redox Catalyst Characterizations

Characterization with XRD

Thorough physicochemical characterizations complemented with detailed simulation studies were employed for in-depth understanding of the redox chemistry and potential reaction pathways. Figure 2a illustrates the XRD patterns of the initial Zn catalyst and the Zn catalyst after STCH of furfural in H_2O and various organic solvent/H_2O mixtures at 150°C. The XRD pattern (Figure 2a) of the initial Zn catalyst is a two-phase mixture consisting of Zn (JCPDS 01-078-7029) and ZnO (JCPDS 00-005-0664), with a Zn percentage of 61.6 wt.% determined by Rietveld refinement (Figure S6, Table. S3). This Zn content is comparable to those obtained from a solar reactor pilot plant via thermal reduction of ZnO[29]. Diffraction peaks attributable to metallic Zn completely disappeared after STCH of furfural in H_2O, cyclohexane/H_2O and dodecane/H_2O mixtures at 150°C, while a trace of Zn (0.6% wt.%) remained in 1,4-Dioxane/H_2O mixture, indicating a complete or near complete oxidation of Zn. After the reaction in CH_2Cl_2/H_2O mixture, peaks associated with $Zn_5(OH)_8Cl_2 \cdot H_2O$ (JCPDS 00-007-0155) were identified aside from ZnO, and the sample showed decreased crystallinity. These results indicate that Zn was oxidized to Zn^{2+} after the reaction. Meanwhile, an interaction between Zn or ZnO with the solvents, e.g., CH_2Cl_2 and H_2O, can occur, producing hydrogen chloride and further reacting with Zn or ZnO. The metallic Zn was partially converted to ZnO even at a low temperature of 25°C in H_2O and different organic solvent/H_2O mixtures (see Figure S7 and Table S3 for more details). This again highlights Zn's superior furfural hydrogenation performance at ambient conditions. Similarly, metallic Zn was partially oxidized after STCH with all the other reactants explored at 25°C (Figure S8). At 150°C, complete oxidation to ZnO was observed in all cases. The possible crystalline phase transition of Fe, Sn, Mn, Mg, Al, AlCu alloy (8% Cu), reduced CeO_2 as well as reduced 1% Ru/CeO_2 catalysts after STCH of furfural in H_2O at 25°C and 150°C were also investigated (see Figure S9-11 for more details). For Fe, Mn, Mg and Al, new reflections identified after reaction at 150°C are indexable to Fe_3O_4, MnO and Mn_3O_4, $Mg(OH)_2$ as well as Al_2O_3 (Figure S9). For the Sn catalyst, a decrease in Sn weight ratio (from 89.0 wt.% to 56.4 wt.%) was observed after reaction at 150°C (Figure S9). For AlCu alloy (8% Cu), reduced CeO_2 and 1% Ru/CeO_2, partial oxidation of the catalysts was evidenced by peak shifts as opposed to appearance of new phases (Figure S9, Figure S10). This shift in 2θ corresponds to an increase in ceria oxidation state and a decrease in oxygen nonstoichiometry ($CeO_{2-\delta} \rightarrow CeO_2$), and a partial oxidation of zero-valent Al. In contrast, there was no apparent structure change observed for Fe, Sn, Mn, Mg, and Al catalysts after the furfural hydrogenation step at 25°C, likely due to the kinetic limitations (Figure S11), which correlates well with the absence of observed furfural conversion at 25°C (Table S1, entries 11-16). To summarize, the XRD analysis indicates that zero-valent metals or surface oxygen vacancies of metal oxide provide the active redox centres and bulk sources of reducing potential for H_2O dissociation and furfural hydrogenation. Such a reaction scheme draws comparison with a recently reported reverse Mars-van Krevelen mechanism[52-54] in terms of lattice oxygen replenishment via oxygen abstraction (from H_2O in this case) and the important role of the coordinatively unsaturated atoms at the interface, as will be discussed in subsequent sections.

Characterization with BET

The textural properties of the Zn catalyst before and after STCH of furfural in neat H_2O, dichloromethane/H_2O and 1,4-Dioxane/H_2O mixtures were further characterized (Figure 2b, Figure S12, Table S4-6). The BET surface area (S_{BET}) of the initial Zn is 4.3 m^2 g^{-1} with a total pore volume of 0.02 cm^{-3} g^{-1} and average pore diameter of 20 nm (Table S4). It is interesting to note that the S_{BET} increased by about 3 times after reaction in neat H_2O at 50 and 100°C (Table S4), as indicated by the enhanced N_2 adsorption in Nitrogen sorption isotherms in Figure 2b. Moreover, a 3 times and even 10 times increase in S_{BET} was observed after reaction in dichloromethane/H_2O mixture at 25 and 50°C, respectively (Table S5). This increase was likely induced by the phase transformation from Zn to ZnO and $Zn_5(OH)_8Cl_2 \cdot H_2O$, as confirmed by XRD patterns and the observed morphological change, which will be discussed later. In 1,4-Dioxane/H_2O mixture, the S_{BET} after reaction was close to the initial Zn catalyst from 25-150°C (Table S6). The S_{BET} decreased in H_2O (3.4 m^2 g^{-1}) and especially in dichloromethane/H_2O mixture (0.2 m^2 g^{-1}) when further increasing to temperature to 150°C (Table S4 and S5). Despite the change in S_{BET} at 150°C, no significant loss in reactivity was observed (Figure S3), suggesting that ionic diffusion in the bulk, as opposed to molecular diffusion at the surface, is the rate controlling step for the oxidation of the Zn catalyst.

Characterization with XPS

The surface elemental states of the Zn catalyst before and after the redox process were characterized by XPS. For the initial Zn catalyst (Figure 2c), two components associated to Zn $2p_{3/2}$ in metallic state (52.3 %) and zinc oxide (47.7 %) were identified with a binding energy of 1021.7 and 1022.2 eV, respectively[55,56]. For the Zn catalyst after reaction in H_2O, a shift toward higher binding energies was observed at 100 and 150ºC with one single component dominant by zinc oxide. This observation is in good agreement with the XRD results and can be explained by the change from metallic zinc to zinc oxide with increasing reaction temperature. Additionally, the O (1s) spectra presented in Figure S13 displayed three contributions located at 530.0, 531.5 and 533.4 eV attributable to lattice oxygen (Zn–O), chemically adsorbed surface oxygen originated from H_2O (Zn–OH) and CO_3 groups (Zn–CO_3)[56,57]. The intensity of the latter contributions increased after reaction in H_2O as compared to the initial Zn catalyst.

Characterization with *In situ* FT-IR

In situ FT-IR measurements were employed to gain molecular insights into the interaction of the reactant with the active site. Literature results show that there are two types of aldehyde chemisorption modes depending on the nature of the metal surface: (1) η^1(O) configuration in which only the carbonyl O is adsorbed on top of a metal atom, or (2) η^2(C,O) configuration where both the C and O interact with the surface[58,59]. For furfural adsorption on metallic Zn, the C=O stretching band ascribed to the η^1(O) mode appears at 1675 cm^{-1}, indicating a vertical aldehyde group adsorption through its terminal O (Figure 2d). Three additional vibration modes were observed, which are assigned to C=C (1568 and 1475 cm^{-1}), C-O-C (1278 and 1078 cm^{-1}), and furfural ring stretching (1020, 930, 883 and 756 cm^{-1})[60,61]. Notably, these bands over ZnO are of much lower intensity, indicating a strong interaction between furfural and the Zn catalyst. The strong interaction of furan and carbonyl groups over metallic Zn may contribute to its superior STCH of furfural performance.

Characterization with SEM

SEM was carried out to investigate the morphological and microstructural changes of Zn catalyst before and after reaction. The initial catalyst was composed of small, nanosized, pyramid-like grains with relatively uniform diameters of 50–100 nm (Figure 2e_1, e_2). Interestingly, for the spent catalysts in H_2O, the pyramid-like grains transformed into conical stake-like crystallites with increased crystal size when the reaction temperature increased to 100 and 150ºC (Figure 3e_3-e_6). It is noteworthy that for the spent catalysts in CH_2Cl_2/H_2O mixture (Figure S14a-d), the pyramid-like grains transformed into platelet-like crystallites with a lateral dimension ranging from 0.1–0.2 µm and a longitudinal dimension between 0.5–4 µm, which contributes to its high surface area as indicated by the BET measurements. The SEM images for the spent catalysts in cyclohexane/H_2O, 1,4-Dioxane/H_2O and dodecane/H_2O mixture are also shown (Figure S15a-c). Similar to the spent catalyst in neat H_2O, the pyramid-like crystallites transformed into conical stake-like crystallites with no pronounced grain growth after reaction.

Characterization with HRTEM-EDX

The elemental distribution and microstructure of the Zn material mixtures were further characterized by HRTEM-EDX. As shown in Figure 3b_1-b_3, HRTEM-EDX mappings of the initial Zn material exhibit a Zn rich region (red) with oxidized ZnO enriched near the surface layer (see Figure S16 for further details). Meanwhile, clear lattice fringes of 0.25 and 0.26 nm corresponding to Zn (002) and ZnO (002) structural domains were revealed (Figure 3c_1, c_2). The above results indicate that the initial Zn is composed of a mixture of Zn and ZnO. For the spent catalyst in H_2O (Figure 3e_1-e_3) as well as in cyclohexane/H_2O mixture (Figure S17), a uniformly distributed Zn (red) and O (green) elements were observed, with well-resolved lattice fringes of 0.26 nm corresponding to ZnO (002) facet. These results reveal that the metallic Zn was completely converted to ZnO after reaction at 150ºC. This agrees well with the XRD analysis. On the other hand, for the spent catalyst in CH_2Cl_2/H_2O mixture (Figure S18), Zn and O were well-dispersed with the presence of Cl in some regions, indicating that the spent catalyst is composed of a mixture of $Zn_5(OH)_8Cl_2\cdot H_2O$ and ZnO. Hence, the above STEM-EDX mapping and HRTEM analysis confirmed that the as-prepared catalyst existed in the form of metallic Zn with oxide enrichment near the surface. It was subsequently transformed into ZnO or $Zn_5(OH)_8Cl_2\cdot H_2O$ and ZnO after STCH of furfural.

DFT Studies

To gain additional fundamental insights, density functional theory (DFT) calculations were carried out to elucidate the reaction landscape of furfural hydrogenation with Zn in water, and ZnO with molecular H_2. Structure models containing both Zn and ZnO phases (see Figure S19), consistent with the XRD, XPS, and HRTEM characterizations, were built and optimized to simulate the Zn catalyst for STCH of furfural. As shown in Figure 4a, water dissociation has a barrier of 0.51 eV on the Zn atom over the ZnO/Zn interface and a negative reaction energy, supporting the hypothesized facile production of atomic H through H_2O dissociation. The generated H adsorbs on the O atom of the ZnO and the remaining OH groups bonded with Zn atoms over the ZnO/Zn interface. In comparison, the barrier for H_2 dissociation on ZnO is 0.64 eV, which is slightly higher than that for H_2O dissociation on the ZnO/Zn interface. More importantly, the subsequent furfural hydrogenation on ZnO/Zn is -0.31 eV exergonic, with an energy barrier of merely 0.62 eV. In comparison, the corresponding step is 1.15 eV endergonic and kinetically hindered with a barrier of 1.40 eV on ZnO with H_2. These results indicate the facile generation of atomic H through H_2O dissociation on ZnO/Zn interface, and the resulting atomic H will preferably react with furfural and its derivatives with low reaction barriers, thus exhibiting superior hydrogenation reactivity for STCH of furfural on Zn. On the other hand, the hydrogenation activity of ZnO with H_2 is hindered by the high energy barrier for furfural hydrogenation. Therefore, the furfural hydrogenation on ZnO/Zn interface in water is kinetically favorable, due to its much lower barrier than that on ZnO (0.62 vs. 1.40 eV), and the furfural hydrogenation on ZnO/Zn interface in water is also thermodynamically favorable over furfural hydrogenation on ZnO with molecular H_2 (-0.31 vs. 1.15 eV). Nakamura et al.[62] investigated the oxidation behaviour of Zn nanoparticles from 110 to 150ºC in air, which showed the oxidation of Zn through rapid outward diffusion across ZnO film by transmission electron microscopy. Hartley et al.[63] demonstrated the Zn migration to the ZnO surface to when reacting with H_2O and CO_2 via micrographs and temperature program reaction study. The DFT calculation indicates a 0.86-1.00 eV energy barrier for the migration of Zn cation vacancies in ZnO (Figure S20). As such, Zn can be relatively easily oxidized to ZnO through outwards diffusion of Zn cations[62,64]. The reaction barriers of atomic H combination for H_2 formation and furfural hydrogenation by atomic H as functions of reaction temperatures were also compared (Figure S21). Results show that the energy barriers of atomic H combination are (~1.1 eV) higher than that of furfural hydrogenation. The difference also slightly decreases with increasing reaction temperature, indicating that an increase in reaction temperature would disproportionally accelerate H combination to produce molecular H_2. This is consistent with experimental observations where furfural conversion and H_2 utilization efficiency peaked at lower reaction temperatures, while the H_2 evolution reaction increased at higher temperatures (Figure S3, Figure S4).

To study the solvent effects on the product selectivity for STCH of furfural, the DFT results in water and in cyclohexane were compared, which correspond to polar and nonpolar solvents, respectively. The energy profiles of furfural hydrogenation reactions over the two solvents are given in Figure 4b. All the reaction intermediates and transition states except FA in the cyclohexane are lower than those in water, suggesting these intermediates are more stabilized in cyclohexane. The stabilization of intermediate product FA is further described by $E_{a,FA} - |E_{ads,FA}|$, in which $E_{a,FA}$ represents the hydrogenation barrier of FA and $E_{ads,FA}$ is the adsorption energy of FA. A larger value of $E_{a,FA} - |E_{ads,FA}|$ indicates higher possibility of the desorption of FA from surface. This method was often adopted in hydrogenation studies.[65,66] The $E_{a,FA} - |E_{ads,FA}|$ difference between water and cyclohexane was calculated to be -0.16 eV, suggesting that FA has a stronger tendency to desorb from the surface in water than in cyclohexane. These results are in good agreement with experiment observations that the selectivity of FA in polar solvents is higher than that in nonpolar solvents. Therefore, solvent polarity may affect the stability of intermediates and transition states, adding an additional degree of freedom to tailor the reactivity and selectivity for STCH of furfural and other oxygenate compounds.

This article demonstrates the feasibility, effectiveness, and underlying mechanism of using water as the atomic hydrogen source for furfural and bio-oils upgrading, through a two-step STCH process facilitated by redox active metals/metal oxides. The STCH process offers the potential to harness renewable energy sources, e.g., solar irradiation or renewable electricity, in the metal oxide reduction step to facilitate the subsequent *in-situ* hydrogen generation and hydrogenation reactions. 7 redox candidates—Zn/ZnO, Sn/SnO, Fe/FeO, Mn/MnO, $CeO_{1.83}/CeO_2$, Mg/MgO and Al/Al_2O_3, were investigated. Furfural was efficiently upgraded at ambient conditions in the presence of Zn with superior hydrogen utilization efficiencies (18.4-51.0% at 25°C), which are 1-2 orders of magnitude higher than molecular-hydrogen-based catalytic hydrogenation (0.1-2.4% over 2% Pd-Ir(Ru, Rh, Pt)/SiO_2 at 25°C, 8 MPa of H_2[67]; 0.8-1.1% over 3% Pd/α-Al_2O_3 at 40°C, 5.52 MPa of H_2[68]). Employing suitable metal/reduced metal oxide catalysts with different oxophilicities, the hydrogenation of furfural can be driven exclusively to FA (Al, AlCu alloy, Mn, Fe and Mg) and 2-MF (reduced CeO_2 and 1%Ru/CeO_2). Solvent was also found to play a crucial role in determining the selectivity: FA was the primary product with high polarity solvents while 2-MF dominates with lower polarity solvents. The STCH scheme was also investigated with various carbonyl substrates besides furfural, exhibiting excellent conversion and selectivity at room temperature and atmospheric pressure. The proposed approach introduces alternative mechanistic pathways to conventional catalytic hydrogenation using molecular H_2, as substantiated by detailed experimental studies and DFT calculations. Specifically, zero-valent metals or reduced metal oxides are shown as a new class of catalysts for STCH, which provide the active sites for furan rings adsorption and a source to dissociate H_2O for *in situ* hydrogen generation. The *in situ* generated reactive H atoms hydrogenate furfural and other biomass-derived oxygenates, eliminating the barriers for H_2 dissolution in the reaction medium and the subsequent dissociation on the catalyst surface. The hydrogenation selectivity can be conveniently mediated by solvents with different polarity and metal/reduced metal oxide catalysts with different oxophilicities, providing additional degrees of freedom in tailoring the product distribution. The two-step STCH approach and the redox active catalysts demonstrated herein can be broadly applicable towards other hydrogenation processes. Therefore, it can open up new possibilities for intensified chemical production while integrating renewable energy sources.

EXPERIMENTAL PROCEDURES

Resource Availability

Lead Contact

Further information and requests for resources and reagents should be directed to and will be fulfilled by the Lead Contact, Fanxing Li (fli5@ncsu.edu).

Materials Availability

This study did not generate new unique materials.

Data and Code Availability

This study did not generate any dataset.

Materials

Furfural (FUR) (99%), furfuryl alcohol (FA) (Analytical standard, ≥99.9%), 2-methylfuran (2-MF) (Analytical standard, ≥99.9%), 2-methyl tetrahydrofuran (2-MTHF) (BioRenewable, anhydrous, ≥99%, inhibitor-free), tetrahydrofurfuryl alcohol (THFA) (Analytical standard, ≥99.9%), tetrahydrofuran (THF) (Certified, ≥99.9%), furan (≥99%), benzaldehyde (ReagentPlus®, 99%), benzyl alcohol (anhydrous, 99.8%), cyclohexanecarboxaldehyde (97%), cyclohexanemethanol (ReagentPlus®, ≥99.0%), cyclohexane (suitable for HPLC, ≥99.9%), cyclohexanone (ACS reagent, ≥99.0%), cyclohexanol (ReagentPlus®, 99%) were of analytical grade and purchased from Sigma-Aldrich.

Catalyst Preparation

Zn (nanopowder, 40-60 nm avg. part. size, ≥99% trace metals basis), Fe (≥99%, power (fine)), Sn (nanopowder, <150 nm particle size (SEM), ≥99% trace metals basis), Al (powder, -325 mesh), Al alloy (8.0% Cu, granularity 5 μm), Mg (powder, ≥99% trace metals basis), Mn (powder, -325 mesh, ≥99% trace metals basis) were purchased from Sigma-Aldrich and used without further treatment. CeO_2 (99.9%) was purchased from Noah Technologies Corporation. Prior to the experiment, the as-received CeO_2 was reduced in 10% H_2/Ar (100 mL/min) at 800ºC for 2 h.

The supported catalyst loaded on CeO_2 with nominal Ru loadings of 1 wt% was prepared via the incipient wetness impregnation method, and is identified as 1Ru/CeO_2. In a typical experiment, 0.05g of $RuCl_3 \cdot xH_2O$ (Sigma-Aldrich, ~40% Ru base) was dissolved in 5 mL deionized water to obtain a homogeneous solution. Subsequently, 2g of support CeO_2 was added and well mixed. The resultant slurry was dried in an oven at 120ºC overnight, followed by calcining at 800ºC (heating rate of 5ºC/min from ambient) under stagnant air for 4 h. Prior to catalytic testing, the supported metal oxide catalysts were reduced in 10% H_2/Ar (100 mL/min) at 800ºC for 2 h, after which it was charged into the reactor.

Catalyst Characterization

X-ray powder diffraction (XRD) patterns were recorded on a Rigaku SmartLab X-ray diffractometer with Cu Kα X-ray radiation (λ = 1.5418 Å), operated at 45 kV and 40 mA. Diffraction profiles were collected in the 2θ range between 10–80º with a step size of 0.02º and a counting time of 40s/step. Phase identification and quantification were conducted based on whole pattern fitting using Rietveld refinement with the PANalytical X'Pert HighScore Plus software. The BET (Brunauer-Emmett-Teller) surface areas (S_{BET}) and pore volumes of the samples were determined via nitrogen sorption in a Micromeritics ASAP 2020 at 77 K. Prior to the measurement, the samples were degassed (< 5 μm Hg) at 200°C for 4 h. The S_{BET} was determined according to the multipoint BET method in the pressure range of P/P_0 = 0.06–0.29. The X-ray photoelectron spectroscopy (XPS) measurements were carried out with a Kratos Analytical AXIS Ultra DLD instrument equipped with a monochromatic Al Kα X-ray source. XPS spectra were recorded at 10 mA and 15 kV, with a pass energy of 20 eV and a step size of 0.1 eV. Deconvolution of the peaks was performed with Casa XPS software (Casa Software Ltd., U.K.) using a Shirley background subtraction and mixed Gaussian–Lorentzian functions. Binding energies were calibrated with C 1s at 284.6 eV. Diffuse reflectance infrared Fourier transform (DRIFT) spectra were performed on a Thermo Scientific Nicolet iS50 FT-IR spectrometer in a Pike DiffusIR cell equipped with a KBr window. Typically, samples were homogenously blended with KBr in a weight ratio of 1:3 and loaded in the alumina crucible. Pretreatment up to 150°C in flowing Ar (30 mL/min) was performed to remove physically adsorbed H_2O and gases, mainly carbon dioxide. The sample was then cooled down to 25°C and a spectrum was collected and used as a background for the following measurements. An Ar carrier gas (30 mL/min) saturated with furfural vapor at room temperature was introduce to the cell for 60 min, followed by purging with Ar for another 60 min at 30 mL/min to remove gaseous and physically adsorbed molecules. The FT-IR spectra were measured at room temperature, accumulating 64 scans with a resolution of 4 cm^{-1}. Surface morphology of the catalyst was investigated on a ThermoFisher Verios 460L Field Emission scanning electron microscopy (SEM) operated at 2 kV. Samples were adhered to conductive carbon tape and secondary electron images were collected without any coating. High-resolution transmission electron microscopy (HRTEM) was performed on a FEI Titan 80-300 transmission electron microscope with a linear resolution of 0.10 nm, which was equipped with a liquid nitrogen cooled energy-dispersive X-ray spectroscopy (EDS) detector for elemental analysis under a working voltage of 200 kV. All samples were crushed into fine powders and dispersed in ethanol by ultrasonication. The suspension was then drop casted onto a holey-carbon coated Cu grid and dried in air under ambient conditions.

Reactivity Evaluation

The reactivity was investigated in a 50 mL stainless-steel batch reactor with an inserted Teflon liner (Parr 4579). The reaction was carried out at 25-150ºC for 4h at a stirring speed of 400 rpm. (i) For furfural hydrogenation with H_2O as the hydrogen donor, the reactor was loaded with 1 mmol of furfural, 15 mL of de-ionized water (13 mL of de-ionized water and 2 mL of 1,4 – Dioxane, or dichloromethane (CH_2Cl_2), or cyclohexane, or dodecane), and 0.4 g of catalyst in each test. Prior to the heating, the reactor was flushed with inert Ar (>99.999%, Air gas) three times before being charged with Ar at 1 atm in absence of hydrogen. (ii) For conventional furfural hydrogenation reactions with H_2, the feedstock was composed of 1 mmol of furfural, 15 mL of de-ionized water (13 mL of de-ionized water and 2 mL of 1,4 – Dioxane, or CH_2Cl_2, or cyclohexane, or dodecane), and 0.4 g of catalyst. After being purged with H_2 (>99.999%, Air gas) three times, the reactor was pressurized to 2 MPa with H_2 and subsequently heated to the set temperature. After reaction and cooling to room temperature, the reactor was depressurized, and the products were filtered and analysed.

The reaction products were analysed by an online gas chromatograph (Agilent model 7820A) equipped with a flame ionization detector (FID) and an J&W DB-5 GC Column (30 m, 0.25 mm, 0.25 μm, 7 inch cage) using an external standard method. Gas chromatograph–mass spectrometry (GC–MS) was performed using an Agilent 7820 GC equipped with a spectrometer operating in the electron-impact mode (EI 70 eV), with an HP-1 MS capillary column (100% dimethylpolysiloxane) installed. The accuracy of the measurement was assured by performing carbon balances.

Carbon balance: moles of C measured in the reactor effluent = mole of C in the feedstock (5)

The furfural conversion and product selectivity are calculated as follows:

$$\text{Furfural conversion} = \frac{\text{Moles of product in the reactor effluent}}{\text{Moles of furfural in the feedstock}} \quad (6)$$

$$\text{Product selectivity} = \frac{\text{Moles of product produced}}{\text{Moles of furfural consumed}} \quad (7)$$

For furfural hydrogenation with H_2O as the hydrogen donor, the hydrogen utilization efficiency is defined as the molar ratio of hydrogen consumed to produce the hydrogenated products per amount of hydrogen produced. The latter is determined by the extent of oxidation of the redox catalyst based on Rietveld refinement of XRD spectra. Using Zn as an example:

$$\text{Hydrogen utilization efficiency} = \frac{\sum_{i=1}^{n} n_i * a_i}{\text{Initial Zn}^0\text{ amount} - \text{Zn}^0\text{ amount after reaction}}$$

$$= \frac{\text{Moles of H}_2\text{ consumed}}{\text{Moles of H}_2\text{ Prodcued}} \quad (8)$$

where n_i donates the mole amount of the hydrogenation product i; a_i donates the stoichiometric coefficient of the corresponding hydrogenation reaction. All the parameters in the above equation are expressed in a H_2-equivalent basis, even though atomic hydrogen is consumed for the hydrogenation reactions in the STCH process.

For conventional furfural hydrogenation reactions with H_2, the hydrogen utilization efficiency can be evaluated as

$$\text{H}_2\text{ utilization efficiency} = \frac{\sum_{i=1}^{n} n_i * a_i}{\text{nH}_2} \quad (9)$$

where nH_2 donates the total amount of H_2 charged in the reactor and can be calculated using the ideal-gas equation of state PV=nRT.

Computational Details

Density functional theory (DFT) calculations within periodic slabs were conducted by Vienna ab initio simulation package (VASP).[69] The generalized gradient approximation (GGA) method was employed to calculate the electronic structures, and the Perdew-Burke-Ernzerhof functional was employed.[70] The calculations utilized the projector-augmented wave (PAW) method to depict the interaction between electrons and atomic cores.[71] The cutoff energy was 450 eV and force convergence criterion was set to 0.05 eV $Å^{-1}$. The lattice parameters of Zn and ZnO were fully optimized; 3-layer 5×5 Zn(001) and 3×2 ZnO($10\bar{1}0$) supercell slabs were built with the bottom layer of atoms fixed and the upmost two layers of atoms and the adsorbates were relaxed during all of the calculations. The ZnO/Zn structure was built by placing extra ZnO clusters onto Zn(001) and, the resulting structure underwent thorough optimizations to obtain a stable structure. The vacuum layer was set larger than 12 Å. All the surface structures have dimensions larger than 10 Å × 10 Å and hence all of the calculations were performed by 2 × 2 × 1 k-point grid. The transition-state structures were obtained by climbing image nudged elastic band (CI-NEB).[72] Vibrational frequency analysis were conducted to characterize the transition state structures and also to calculate the zero-point energies. Solvent effects significantly affect the catalytic activity,[73,74] thus here the implicit solvation models by VASPsol were used to describe the interaction between solvents and sorbents.[75] The dielectric constants were 80 for water and 2 for cyclohexane solvents, and the water and cyclohexane represent polar and nonpolar solvents, respectively.

Acknowledgements

This work was supported by the U.S. National Science Foundation (Award No. CBET- 2116724 and CBET- 1923468) and the Kenan Institute for Engineering, Technology and Science at NC State University. We acknowledge the computing resources provided by North Carolina State University High Performance Computing Services Core Facility (RRID: SCR_022168).

Author contributions

C.R. analysed the data and wrote the paper. R.A. and N.M.Z. conducted the experimental studies and assisted with the data analysis. K.Y. conducted the DFT calculations and writing. J.D. and A.B. contributed to experimental setup design and product identification. J.L performance the XPS measurement. L.B. and H.H.L. contributed to the discussion. F.L conceived this project and revised the manuscript. All authors discussed the results and commented on the manuscript.

DECLARATION OF INTERESTS

The authors declare no competing financial interest.

Figure 1. Thermodynamic and reaction performance of STCH of furfural

(a) Variations of Gibbs free energy for H_2O splitting with metal or reduced metal oxide (metal/reduced metal oxide + $2H_2O \rightarrow$ metal oxide + $2H_2$) as a function of temperature at 1 bar. (b) Conversion and furanic product selectivity for STCH of furfural over Zn catalyst in neat H_2O, 1,4-Dioxane/H_2O, dichloromethane/H_2O, cyclohexane/H_2O, dodecane/H_2O mixture (2 mL H_2O, 13 mL organic solvent) at 25°C and 1 atm of Ar. (c) Furanic product yield and H_2 utilization efficiency of Zn sample for STCH of furfural as compared with the conventional molecular-hydrogen-based hydrogenation process over ZnO catalyst (2 MPa H_2) in neat H_2O, 1,4-Dioxane/H_2O mixture and dichloromethane/H_2O mixture at 150°C. Furanic product yield and H_2 utilization efficiency of ZnO catalyst in H_2O medium at 150°C (1 atm of Ar) are also included. Error bars represent the standard deviation from three independent measurements. (d) Comparison of hydrogen utilization efficiency for STCH of furfural over Zn catalyst with the state-of-the-art catalysts in either the liquid or gas phases employing molecular hydrogen as the reducing agent. I, ref.[67]; II, ref.[76]; III, ref.[68]; IV, ref.[77]; V, ref[78]; VI, ref[79]; VII, ref[80]; VIII, ref[81]; IX, ref[47]; X, ref[82]; XI, ref[83]; XII, ref[84]; XIII, ref[85]; XIV, ref[86]; XV, ref[87]. See Table S2 for more details.

Figure 2. Physicochemical characterizations of Zn catalyst before and after STCH of furfural

(a) X-ray powder diffraction patterns of Zn catalyst before and after STCH of furfural in neat H_2O, 1,4-Dioxane/H_2O, cyclohexane/H_2O, dodecane/H_2O, dichloromethane/H_2O mixture (2 mL H_2O, 13 mL organic solvent) at 150°C. (b) N_2 adsorption−desorption isotherms of Zn catalyst before and after reaction in neat H_2O from 25 to 150°C. (c) High-resolution Zn *2p3/2* XPS spectra of initial Zn catalyst before and after STCH of furfural in H_2O from 25 to 150°C. (d) DRIFT spectra of furfural adsorbed on Zn and ZnO catalysts. Insert shows the furfural adsorption through η^1(O) configuration. Colour code: Zn (light grey), O (red), C (dark gray) and H (white). Representative SEM images of Zn catalyst before (e_1, e_2) and after STCH of furfural in neat H_2O at (e_3) 25°C, (e_4) 50°C, (e_5) 100°C and (e_6) 150°C. Scale bars in the images represent 1μm unless otherwise noted.

Figure 3. Structure and element distributions of initial Zn and Zn catalyst after STCH of furfural in neat H_2O at 150°C

(a) Representative STEM image and the corresponding element-mapping images of (b_1) Zn, (b_2) O and (b_3) combination of Zn and O for the initial Zn catalyst. (c) HRTEM image of the initial Zn catalyst; (c_1, c_2) HRTEM images of the initial Zn catalyst of regions 1 and 2 in c. (d) Representative STEM image and the corresponding elemental-mapping images of (e_1) Zn, (e_2) O and (e_3) combination of Zn and O for Zn catalyst after STCH of furfural in neat H_2O at 150°C. (f) HRTEM image of Zn catalyst after STCH of furfural in neat H_2O at 150°C, along with the respective FFT pattern characteristics of ZnO; (c_1, c_2) HRTEM image of spent Zn catalyst of regions 1 in f.

Figure 4. Energy profile of furfural hydrogenation via Density functional theory (DFT) calculations

(a) Energy profile of H production through H_2O/H_2 dissociation and the subsequent furfural hydrogenation by the produced H. Red line indicates water dissociation on ZnO/Zn structure while black line indicates the H_2 dissociation on ZnO structure. The structures of corresponding states are given. The calculations are based on water solvent. (b) Energy profile of furfural hydrogenation to 2-methylfuran (2-MF) under water (black line) and cyclohexane (blue line). Colour code: Zn (grey), O (red), C (brown), H (pink). Energy unit in eV.

Table 1. Catalytic activity of Zn for two-step STCH of various carbonyl containing reactants. Reaction conditions: 4 h, 150°C, 1 atm of Ar, 0.4 g of catalyst, 1mmol of reactant and 15 mL H_2O

Entry	Catalyst	Substrate	Product	Temp. (°C)	Conv. (%)	Sele. (%)
1	Zn	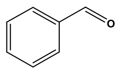	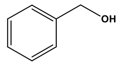	25	>99	>99
2	Zn	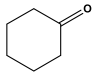	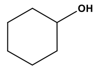	25	9.7	>99
3	Zn	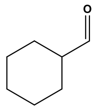	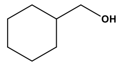	25	>99	>99
4	Zn	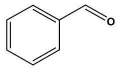	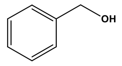	150	96	>99
5	Zn	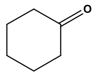	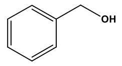	150	19	>99
6	Zn	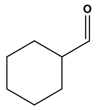	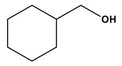	150	73	>99

References

1. McGlade, C., and Ekins, P. (2015). The geographical distribution of fossil fuels unused when limiting global warming to 2 degrees C. Nature *517*, 187-190. 10.1038/nature14016.
2. Davis, S.J., Lewis, N.S., Shaner, M., Aggarwal, S., Arent, D., Azevedo, I.L., Benson, S.M., Bradley, T., Brouwer, J., Chiang, Y.M., et al. (2018). Net-zero emissions energy systems. Science *360*. 10.1126/science.aas9793.
3. Lewis, N.S. (2016). Research opportunities to advance solar energy utilization. Science *351*, **1920-1929**. 10.1126/science.aad1920.

4. Chu, S., and Majumdar, A. (2012). Opportunities and challenges for a sustainable energy future. Nature *488*, 294-303. 10.1038/nature11475.
5. Leitner, W., Klankermayer, J., Pischinger, S., Pitsch, H., and Kohse-Hoinghaus, K. (2017). Advanced Biofuels and Beyond: Chemistry Solutions for Propulsion and Production. Angew. Chem., Int. Ed. *56*, 5412-5452. 10.1002/anie.201607257.
6. Stocker, M. (2008). Biofuels and biomass-to-liquid fuels in the biorefinery: catalytic conversion of lignocellulosic biomass using porous materials. Angew. Chem., Int. Ed. *47*, 9200-9211. 10.1002/anie.200801476.
7. Huber, G.W., Iborra, S., and Corma, A. (2006). Synthesis of transportation fuels from biomass: Chemistry, catalysts, and engineering. Chem. Rev *106*, 4044-4098. 10.1021/cr068360d.
8. Huber, G.W., and Corma, A. (2007). Synergies between bio- and oil refineries for the production of fuels from biomass. Angew. Chem., Int. Ed. *46*, 7184-7201. 10.1002/anie.200604504.
9. Saidi, M., Samimi, F., Karimipourfard, D., Nimmanwudipong, T., Gates, B.C., and Rahimpour, M.R. (2014). Upgrading of lignin-derived bio-oils by catalytic hydrodeoxygenation. Energy Environ. Sci. *7*, 103-129. 10.1039/c3ee43081b.
10. Sun, Z., Bottari, G., Afanasenko, A., Stuart, M.C.A., Deuss, P.J., Fridrich, B., and Barta, K. (2018). Complete lignocellulose conversion with integrated catalyst recycling yielding valuable aromatics and fuels. Nature Catalysis *1*, 82-92. 10.1038/s41929-017-0007-z.
11. Zakzeski, J., Bruijnincx, P.C.A., Jongerius, A.L., and Weckhuysen, B.M. (2010). The Catalytic Valorization of Lignin for the Production of Renewable Chemicals. Chem. Rev *110*, 3552-3599. 10.1021/cr900354u.
12. Green, S.K., Lee, J., Kim, H.J., Tompsett, G.A., Kim, W.B., and Huber, G.W. (2013). The electrocatalytic hydrogenation of furanic compounds in a continuous electrocatalytic membrane reactor. Green Chemistry *15*, 1869. 10.1039/c3gc00090g.
13. Mariscal, R., Maireles-Torres, P., Ojeda, M., Sádaba, I., and López Granados, M. (2016). Furfural: a renewable and versatile platform molecule for the synthesis of chemicals and fuels. Energy Environ. Sci. *9*, 1144-1189. 10.1039/c5ee02666k.
14. Xing, R., Qi, W., and Huber, G.W. (2011). Production of furfural and carboxylic acids from waste aqueous hemicellulose solutions from the pulp and paper and cellulosic ethanol industries. Energy Environ. Sci. *4*, 2193. 10.1039/c1ee01022k.
15. Xu, C., Paone, E., Rodriguez-Padron, D., Luque, R., and Mauriello, F. (2020). Recent catalytic routes for the preparation and the upgrading of biomass derived furfural and 5-hydroxymethylfurfural. Chem Soc Rev *49*, 4273-4306. 10.1039/d0cs00041h.
16. Lange, J.P., van der Heide, E., van Buijtenen, J., and Price, R. (2012). Furfural--a promising platform for lignocellulosic biofuels. ChemSusChem *5*, 150-166. 10.1002/cssc.201100648.
17. Li, X., Jia, P., and Wang, T. (2016). Furfural: A Promising Platform Compound for Sustainable Production of C4 and C5 Chemicals. ACS Catal. *6*, 7621-7640. 10.1021/acscatal.6b01838.
18. Yan, K., Wu, G., Lafleur, T., and Jarvis, C. (2014). Production, properties and catalytic hydrogenation of furfural to fuel additives and value-added chemicals. Renewable and Sustainable Energy Reviews *38*, 663-676. 10.1016/j.rser.2014.07.003.
19. Karinen, R., Vilonen, K., and Niemela, M. (2011). Biorefining: heterogeneously catalyzed reactions of carbohydrates for the production of furfural and hydroxymethylfurfural. ChemSusChem *4*, 1002-1016. 10.1002/cssc.201000375.
20. Nakagawa, Y., Tamura, M., and Tomishige, K. (2013). Catalytic Reduction of Biomass-Derived Furanic Compounds with Hydrogen. ACS Catal. *3*, 2655-2668. 10.1021/cs400616p.
21. Gilkey, M.J., Panagiotopoulou, P., Mironenko, A.V., Jenness, G.R., Vlachos, D.G., and Xu, B. (2015). Mechanistic Insights into Metal Lewis Acid-Mediated Catalytic Transfer Hydrogenation of Furfural to 2-Methylfuran. ACS Catal. *5*, 3988-3994. 10.1021/acscatal.5b00586.
22. Gilkey, M.J., and Xu, B. (2016). Heterogeneous Catalytic Transfer Hydrogenation as an Effective Pathway in Biomass Upgrading. ACS Catal. *6*, 1420-1436. 10.1021/acscatal.5b02171.
23. Nilges, P., and Schröder, U. (2013). Electrochemistry for biofuel generation: production of furans by electrocatalytic hydrogenation of furfurals. Energy Environ. Sci. *6*, 2925. 10.1039/c3ee41857j.
24. Delima, R.S., Stankovic, M.D., MacLeod, B.P., Fink, A.G., Rooney, M.B., Huang, A., Jansonius, R.P., Dvorak, D.J., and Berlinguette, C.P. (2022). Selective hydrogenation of furfural using a membrane reactor. Energy Environ. Sci. *15*, 215-224. 10.1039/d1ee02818a.
25. Chueh, W.C., C., F., Abbott M., D., S., P., F., Haile, S.M., and Steinfeld, A. (2010). High-Flux Solar-Driven Thermochemical Dissociation of CO_2 and H_2O Using Nonstoichiometric Ceria. Science *330*, 1797-1801. 10.1126/science.1198374.
26. Muhich, C.L., Evanko, B.W., Weston, K.C., Lichty, P., Liang, X., Martinek, J., Musgrave, C.B., and Weimer, A.W. (2013). Efficient generation of H_2 by splitting water with an isothermal redox cycle. Science *341*, 540-542. 10.1126/science.1239454.
27. Roeb, M., and Sattler, C. (2013). Isothermal water splitting. Science *341*, 470-471. 10.1126/science.1241311.
28. Krenzke, P., Krueger, K., Leonard, N., Duncan, S., Palumbo, R.D., and Möller, S. (2010). A Solar Thermal Electrolytic Reactor for Studying the Production of Metals From Their Oxides. Journal of Solar Energy Engineering *132*. 10.1115/1.4001464.
29. Koepf, E., Villasmil, W., and Meier, A. (2016). Pilot-scale solar reactor operation and characterization for fuel production via the Zn/ZnO thermochemical cycle. Applied Energy *165*, 1004-1023. 10.1016/j.apenergy.2015.12.106.
30. Zhu, X., Imtiaz, Q., Donat, F., Müller, C.R., and Li, F. (2020). Chemical looping beyond combustion – a perspective. Energy Environ. Sci. 10.1039/c9ee03793d.
31. Wang, X., Gao, Y., Krzystowczyk, E., Iftikhar, S., Dou, J., Cai, R., Wang, H., Ruan, C., Ye, S., and Li, F. (2022). High-throughput oxygen chemical potential engineering of perovskite oxides for chemical looping applications. Energy Environ. Sci. *15*, 1512-1528. 10.1039/d1ee02889h.
32. Metcalfe, I.S., Ray, B., Dejoie, C., Hu, W., de Leeuwe, C., Dueso, C., Garcia-Garcia, F.R., Mak, C.M., Papaioannou, E.I., Thompson, C.R., and Evans, J.S.O. (2019). Overcoming chemical equilibrium limitations using a thermodynamically reversible chemical reactor. Nat. Chem. *11*, 638-643. 10.1038/s41557-019-0273-2.
33. Warren, K.J., Tran, J.T., and Weimer, A.W. (2022). A thermochemical study of iron aluminate-based materials: a preferred class for isothermal water splitting. Energy Environ. Sci. *15*, 806-821. 10.1039/d1ee02679h.
34. Carrillo, A.J., Bork, A.H., Moser, T., Sediva, E., Hood, Z.D., and Rupp, J.L.M. (2019). Modifying $La_{0.6}Sr_{0.4}MnO_3$ Perovskites with Cr Incorporation for Fast Isothermal CO_2-Splitting Kinetics in Solar-Driven Thermochemical Cycles. Advanced Energy Materials, 1803886. 10.1002/aenm.201803886.

35. Fletcher, E.A. (1999). Solarthermal and solar quasi-electrolytic processing and separations: Zinc from zinc oxide as an example. Industrial & Engineering Chemistry Research *38*, 2275-2282. 10.1021/ie990053t.
36. Chambon, M., Abanades, S., and Flamant, G. (2011). Thermal dissociation of compressed ZnO and SnO_2 powders in a moving-front solar thermochemical reactor. AIChE J. *57*, 2264-2273. 10.1002/aic.12432.
37. Charvin, P., Abanades, S., Lemont, F., and Flamant, G. (2008). Experimental study of SnO_2/SnO/Sn thermochemical systems for solar production of hydrogen. AIChE J. *54*, 2759-2767. 10.1002/aic.11584.
38. Abanades, S., Charvin, P., and Flamant, G. (2007). Design and simulation of a solar chemical reactor for the thermal reduction of metal oxides: Case study of zinc oxide dissociation. Chemical Engineering Science *62*, 6323-6333. 10.1016/j.ces.2007.07.042.
39. Chambon, M., Abanades, S., and Flamant, G. (2010). Solar thermal reduction of ZnO and SnO_2: Characterization of the recombination reaction with O_2. Chemical Engineering Science *65*, 3671-3680. 10.1016/j.ces.2010.03.005.
40. Schappi, R., Rutz, D., Dahler, F., Muroyama, A., Haueter, P., Lilliestam, J., Patt, A., Furler, P., and Steinfeld, A. (2022). Drop-in fuels from sunlight and air. Nature *601*, 63-68. 10.1038/s41586-021-04174-y.
41. Ruan, C., Huang, Z.-Q., Lin, J., Li, L., Liu, X., Tian, M., Huang, C., Chang, C.-R., Li, J., and Wang, X. (2019). Synergy of the catalytic activation on Ni and the CeO2–TiO2/Ce2Ti2O7 stoichiometric redox cycle for dramatically enhanced solar fuel production. Energy Environ. Sci. *12*, 767-779. 10.1039/c8ee03069c.
42. Ruan, C., Tan, Y., Li, L., Wang, J., Liu, X., and Wang, X. (2017). A novel CeO_2-xSnO_2/$Ce_2Sn_2O_7$ pyrochlore cycle for enhanced solar thermochemical water splitting. AIChE J. *63*, 3450-3462. 10.1002/aic.15701.
43. Marxer, D., Furler, P., Takacs, M., and Steinfeld, A. (2017). Solar thermochemical splitting of CO_2 into separate streams of CO and O_2 with high selectivity, stability, conversion, and efficiency. Energy Environ. Sci. *10*, 1142-1149. 10.1039/c6ee03776c.
44. Tou, M., Michalsky, R., and Steinfeld, A. (2017). Solar-Driven Thermochemical Splitting of CO_2 and In Situ Separation of CO and O_2 across a Ceria Redox Membrane Reactor. Joule, 146-154. 10.1016/j.joule.2017.07.015.
45. Aldosari, O.F., Iqbal, S., Miedziak, P.J., Brett, G.L., Jones, D.R., Liu, X., Edwards, J.K., Morgan, D.J., Knight, D.K., and Hutchings, G.J. (2016). Pd–Ru/TiO2 catalyst – an active and selective catalyst for furfural hydrogenation. Catalysis Science & Technology *6*, 234-242. 10.1039/c5cy01650a.
46. Iqbal, S., Liu, X., Aldosari, O.F., Miedziak, P.J., Edwards, J.K., Brett, G.L., Akram, A., King, G.M., Davies, T.E., Morgan, D.J., et al. (2014). Conversion of furfuryl alcohol into 2-methylfuran at room temperature using Pd/TiO2 catalyst. Catal. Sci. Technol. *4*, 2280-2286. 10.1039/c4cy00184b.
47. Nguyen-Huy, C., Lee, J., Seo, J.H., Yang, E., Lee, J., Choi, K., Lee, H., Kim, J.H., Lee, M.S., Joo, S.H., et al. (2019). Structure-dependent catalytic properties of mesoporous cobalt oxides in furfural hydrogenation. Appl. Catal. A *583*, 117125. 10.1016/j.apcata.2019.117125.
48. Islam, M.J., Granollers Mesa, M., Osatiashtiani, A., Manayil, J.C., Isaacs, M.A., Taylor, M.J., Tsatsos, S., and Kyriakou, G. (2021). PdCu single atom alloys supported on alumina for the selective hydrogenation of furfural. Applied Catalysis B: Environmental *299*, 120652. 10.1016/j.apcatb.2021.120652.
49. Tang, F., Wang, L., Dessie Walle, M., Mustapha, A., and Liu, Y.-N. (2020). An alloy chemistry strategy to tailoring the d-band center of Ni by Cu for efficient and selective catalytic hydrogenation of furfural. Journal of Catalysis *383*, 172-180. 10.1016/j.jcat.2020.01.019.
50. Venstrom, L., Krueger, K., Leonard, N., Tomlinson, B., Duncan, S., and Palumbo, R.D. (2009). Solar Thermal Electrolytic Process for the Production of Zn From ZnO: An Ionic Conductivity Study. Journal of Solar Energy Engineering-Transactions of the Asme *131*, 031005. 10.1115/1.3142802.
51. Steinfeld, A. (2002). Solar hydrogen production via a two-step water-splitting thermochemical cycle based on Zn/ZnO redox reactions. Int. J. Hydrogen Energy *27*, 611-619, Pii s0360-3199(01)00177-x. 10.1016/s0360-3199(01)00177-x.
52. Mironenko, A.V., and Vlachos, D.G. (2016). Conjugation-Driven "Reverse Mars-van Krevelen"-Type Radical Mechanism for Low-Temperature C-O Bond Activation. J. Am. Chem. Soc. *138*, 8104-8113. 10.1021/jacs.6b02871.
53. Goulas, K.A., Mironenko, A.V., Jenness, G.R., Mazal, T., and Vlachos, D.G. (2019). Fundamentals of C–O bond activation on metal oxide catalysts. Nature Catalysis *2*, 269-276. 10.1038/s41929-019-0234-6.
54. Fu, J., Lym, J., Zheng, W., Alexopoulos, K., Mironenko, A.V., Li, N., Boscoboinik, J.A., Su, D., Weber, R.T., and Vlachos, D.G. (2020). C–O bond activation using ultralow loading of noble metal catalysts on moderately reducible oxides. Nature Catalysis *3*, 446-453. 10.1038/s41929-020-0445-x.
55. Feliu, S., and Barranco, V. (2003). XPS study of the surface chemistry of conventional hot-dip galvanised pure Zn, galvanneal and Zn–Al alloy coatings on steel. Acta Mater. *51*, 5413-5424. 10.1016/s1359-6454(03)00408-7.
56. Diler, E., Rioual, S., Lescop, B., Thierry, D., and Rouvellou, B. (2012). Chemistry of corrosion products of Zn and MgZn pure phases under atmospheric conditions. Corrosion Science *65*, 178-186. 10.1016/j.corsci.2012.08.014.
57. Roiaz, M., Monachino, E., Dri, C., Greiner, M., Knop-Gericke, A., Schlogl, R., Comelli, G., and Vesselli, E. (2016). Reverse Water-Gas Shift or Sabatier Methanation on Ni(110)? Stable Surface Species at Near-Ambient Pressure. J. Am. Chem. Soc. *138*, 4146-4154. 10.1021/jacs.5b13366.
58. Mavrikakis, M., and Barteau, M.A. (1998). Oxygenate reaction pathways on transition metal surfaces. Journal of Molecular Catalysis a-Chemical *131*, 135-147. 10.1016/s1381-1169(97)00261-6.
59. Avery, N.R. (1983). EELS IDENTIFICATION OF THE ADSORBED SPECIES FROM ACETONE ADSORPTION ON PT(111). Surf. Sci. *125*, 771-786. 10.1016/s0039-6028(83)80059-4.
60. Rogojerov, M., Keresztury, G., and Jordanov, B. (2005). Vibrational spectra of partially oriented molecules having two conformers in nematic and isotropic solutions: furfural and 2-chlorobenzaldehyde. Spectrochimica acta. Part A, Molecular and biomolecular spectroscopy *61*, 1661-1670. 10.1016/j.saa.2004.11.043.
61. Wang, Q., Feng, J., Zheng, L., Wang, B., Bi, R., He, Y., Liu, H., and Li, D. (2019). Interfacial Structure-Determined Reaction Pathway and Selectivity for 5-(Hydroxymethyl)furfural Hydrogenation over Cu-Based Catalysts. ACS Catal. *10*, 1353-1365. 10.1021/acscatal.9b03630.
62. Nakamura, R., Lee, J.G., Tokozakura, D., Mori, H., and Nakajima, H. (2007). Formation of hollow ZnO through low-temperature oxidation of Zn nanoparticles. Materials Letters *61*, 1060-1063. 10.1016/j.matlet.2006.06.039.

63. Tongnan, V., Sornchamni, T., Laosiripojana, N., and Hartley, U.W. (2018). Study of crystal growth and kinetic parameters of Zn/ZnO oxidation in the presence of H2O and CO2. Reaction Kinetics, Mechanisms and Catalysis *125*, 99-110. 10.1007/s11144-018-1411-3.
64. Weibel, D., Jovanovic, Z.R., Galvez, E., and Steinfeld, A. (2014). Mechanism of Zn Particle Oxidation by H(2)O and CO(2) in the Presence of ZnO. Chem Mater *26*, 6486-6495. 10.1021/cm503064f.
65. Yang, K., and Yang, B. (2018). Identification of the Active and Selective Sites over a Single Pt Atom-Alloyed Cu Catalyst for the Hydrogenation of 1,3-Butadiene: A Combined DFT and Microkinetic Modeling Study. J. Phys. Chem. C *122*, 10883-10891. 10.1021/acs.jpcc.8b01980.
66. Yang, K., and Yang, B. (2017). Surface Restructuring of Cu-based Single-atom Alloy Catalysts under Reaction Conditions: The Essential Role of Adsorbates. Phys. Chem. Chem. Phys. *19*, 18010-18017. 10.1039/C7CP02152F.
67. Nakagawa, Y., Takada, K., Tamura, M., and Tomishige, K. (2014). Total Hydrogenation of Furfural and 5-Hydroxymethylfurfural over Supported Pd–Ir Alloy Catalyst. ACS Catal. *4*, 2718-2726. 10.1021/cs500620b.
68. Zhao, Z., Bababrik, R., Xue, W., Li, Y., Briggs, N.M., Nguyen, D.-T., Nguyen, U., Crossley, S.P., Wang, S., Wang, B., and Resasco, D.E. (2019). Solvent-mediated charge separation drives alternative hydrogenation path of furanics in liquid water. Nature Catalysis *2*, 431-436. 10.1038/s41929-019-0257-z.
69. Kresse, G., and Furthmüller, J. (1996). Efficient iterative schemes for ab initio total-energy calculations using a plane-wave basis set. Phys. Rev. B *54*, 11169-11186. 10.1103/PhysRevB.54.11169.
70. Perdew, J.P., Burke, K., and Ernzerhof, M. (1996). Generalized Gradient Approximation Made Simple. Phys. Rev. Lett. *77*, 3865-3868. 10.1103/PhysRevLett.77.3865.
71. Blöchl, P.E. (1994). Projector augmented-wave method. Phys. Rev. B *50*, 17953-17979. 10.1103/PhysRevB.50.17953.
72. Henkelman, G., Uberuaga, B.P., and Jónsson, H. (2000). A climbing image nudged elastic band method for finding saddle points and minimum energy paths. J. Chem. Phys. *113*, 9901-9904. 10.1063/1.1329672.
73. Yang, K., Liu, J., and Yang, B. (2021). Mechanism and Active Species in NH3 Dehydrogenation under an Electrochemical Environment: An Ab Initio Molecular Dynamics Study. ACS Catal. *11*, 4310-4318. 10.1021/acscatal.0c05247.
74. Yang, K., Liu, J., and Yang, B. (2022). Electrocatalytic oxidation of ammonia on Pt: Mechanistic insights into the formation of N2 in alkaline media. J. Catal. *405*, 626-633. https://doi.org/10.1016/j.jcat.2021.10.029.
75. Mathew, K., Sundararaman, R., Letchworth-Weaver, K., Arias, T.A., and Hennig, R.G. (2014). Implicit solvation model for density-functional study of nanocrystal surfaces and reaction pathways. J. Chem. Phys. *140*, 084106. 10.1063/1.4865107.
76. Wu, J., Gao, G., Li, J., Sun, P., Long, X., and Li, F. (2017). Efficient and versatile CuNi alloy nanocatalysts for the highly selective hydrogenation of furfural. Applied Catalysis B: Environmental *203*, 227-236. 10.1016/j.apcatb.2016.10.038.
77. Deng, Y., Gao, R., Lin, L., Liu, T., Wen, X.D., Wang, S., and Ma, D. (2018). Solvent Tunes the Selectivity of Hydrogenation Reaction over alpha-MoC Catalyst. J. Am. Chem. Soc. *140*, 14481-14489. 10.1021/jacs.8b09310.
78. Tamura, M., Tokonami, K., Nakagawa, Y., and Tomishige, K. (2013). Rapid synthesis of unsaturated alcohols under mild conditions by highly selective hydrogenation. Chem Commun (Camb) *49*, 7034-7036. 10.1039/c3cc41526k.
79. Liu, S., Amada, Y., Tamura, M., Nakagawa, Y., and Tomishige, K. (2014). One-pot selective conversion of furfural into 1,5-pentanediol over a Pd-added Ir–ReOx/SiO2bifunctional catalyst. Green Chem. *16*, 617-626. 10.1039/c3gc41335g.
80. Hronec, M., and Fulajtarová, K. (2012). Selective transformation of furfural to cyclopentanone. Catalysis Communications *24*, 100-104. 10.1016/j.catcom.2012.03.020.
81. Weerachawanasak, P., Krawmanee, P., Inkamhaeng, W., Cadete Santos Aires, F.J., Sooknoi, T., and Panpranot, J. (2021). Development of bimetallic Ni-Cu/SiO2 catalysts for liquid phase selective hydrogenation of furfural to furfuryl alcohol. Catalysis Communications *149*, 106221. 10.1016/j.catcom.2020.106221.
82. Pino, N., Sitthisa, S., Tan, Q., Souza, T., López, D., and Resasco, D.E. (2017). Structure, activity, and selectivity of bimetallic Pd-Fe/SiO2 and Pd-Fe/γ-Al2O3 catalysts for the conversion of furfural. Journal of Catalysis *350*, 30-40. 10.1016/j.jcat.2017.03.016.
83. Nakagawa, Y., Nakazawa, H., Watanabe, H., and Tomishige, K. (2012). Total Hydrogenation of Furfural over a Silica‐Supported Nickel Catalyst Prepared by the Reduction of a Nickel Nitrate Precursor. ChemCatChem *4*, 1791-1797. 10.1002/cctc.201200218.
84. Sitthisa, S., Pham, T., Prasomsri, T., Sooknoi, T., Mallinson, R.G., and Resasco, D.E. (2011). Conversion of furfural and 2-methylpentanal on Pd/SiO2 and Pd–Cu/SiO2 catalysts. Journal of Catalysis *280*, 17-27. 10.1016/j.jcat.2011.02.006.
85. Zheng, H.-Y., Zhu, Y.-L., Teng, B.-T., Bai, Z.-Q., Zhang, C.-H., Xiang, H.-W., and Li, Y.-W. (2006). Towards understanding the reaction pathway in vapour phase hydrogenation of furfural to 2-methylfuran. Journal of Molecular Catalysis A: Chemical *246*, 18-23. 10.1016/j.molcata.2005.10.003.
86. Hutchings, G.S., Luc, W., Lu, Q., Zhou, Y., Vlachos, D.G., and Jiao, F. (2017). Nanoporous Cu–Al–Co Alloys for Selective Furfural Hydrodeoxygenation to 2-Methylfuran. Industrial & Engineering Chemistry Research *56*, 3866-3872. 10.1021/acs.iecr.7b00316.
87. Sheng, H., and Lobo, R.F. (2016). Iron-Promotion of Silica-Supported Copper Catalysts for Furfural Hydrodeoxygenation. ChemCatChem *8*, 3402-3408. 10.1002/cctc.201600540.